LETTER

Field-effect conductivity scaling for two-dimensional materials with tunable impurity density

To cite this article: Chulin Wang *et al* 2022 *2D Mater.* **9** 031002

View the article online for updates and enhancements.

You may also like

- Mathematical analysis of some couplings for the Eddington-inspired-Born-Infeld theory of bi-gravity in Bondi coordinates
Calvin Tadmon and Guichard Djiodjo-Seugmo
- Critical temperature of chiral symmetry restoration for quark matter with a chiral chemical potential
M Ruggieri and G X Peng
- High temperature magnetic order in $Zn_{1-x}Mn_xSnSb_2$+MnSb nanocomposite ferromagnetic semiconductors
L Kilanski, M Górska, A lawska-Waniewska et al.

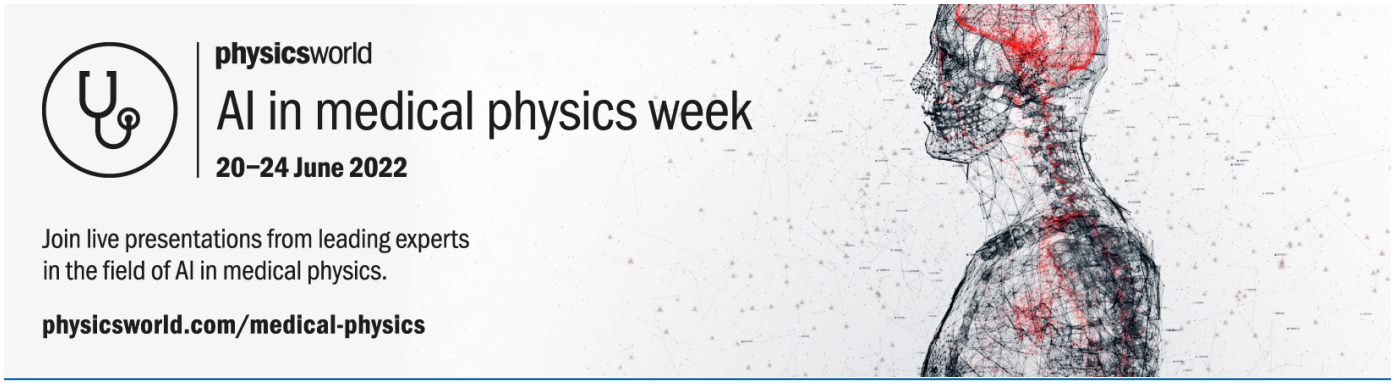

This content was downloaded from IP address 165.124.85.79 on 16/06/2022 at 18:53

2D Materials

LETTER

Field-effect conductivity scaling for two-dimensional materials with tunable impurity density

Chulin Wang[1], Lintao Peng[2], Spencer A Wells[3], Jeffrey D Cain[3], Yi-Kai Huang[3], Lawrence A Rhoads[2], Vinayak P Dravid[2,3], Mark C Hersam[1,2,3,4] and Matthew A Grayson[1,2,*]

[1] Department of Electrical and Computer Engineering, Northwestern University, Evanston, IL 60208, United States of America
[2] Applied Physics Graduate Program, Northwestern University, Evanston, IL 60208, United States of America
[3] Department of Materials Science and Engineering, Northwestern University, Evanston, IL 60208, United States of America
[4] Department of Chemistry, Northwestern University, Evanston, IL 60208, United States of America
[*] Author to whom any correspondence should be addressed.

E-mail: m-grayson@northwestern.edu

RECEIVED
24 February 2022

REVISED
11 May 2022

ACCEPTED FOR PUBLICATION
24 May 2022

PUBLISHED
16 June 2022

Keywords: 2D electronics, ionized impurities, negative bias instability, electronic transport, black phosphorous, bismuth selenide, deep-level transient spectroscopy

Supplementary material for this article is available online

Abstract

A scaling law is demonstrated in the conductivity of gated two-dimensional (2D) materials with tunable concentrations of ionized impurity scatterers. Experimental data is shown to collapse onto a single 2D conductivity scaling (2DCS) curve when the mobility is scaled by r, the relative impurity-induced scattering, and the gate voltage is shifted by V_s, a consequence of impurity-induced doping. This 2DCS analysis is demonstrated first in an encapsulated 2D black phosphorus multilayer at $T = 100\,\mathrm{K}$ with charge trap densities programmed by a gate bias upon cooldown, and next in a Bi_2Se_3 2D monolayer at room temperature exposed to varying concentrations of gas adsorbates. The observed scaling can be explained using a conductivity model with screened ionized impurity scatterers. The slope of the r vs. V_s plot defines a disorder-charge specific scattering rate $\Gamma_q = \mathrm{d}r/\mathrm{d}V_s$ equivalent to a scattering strength per unit impurity charge density: $\Gamma_q > 0$ indicates a preponderance of positively charged impurities with $\Gamma_q < 0$ for negatively charged. This 2DCS analysis is expected to be applicable in arbitrary 2D materials systems with tunable impurity density, which will advance 2D materials characterization and improve performance of 2D sensors and transistors.

Since the advent of graphene as a two-dimensional (2D) material, many other promising layered 2D materials have been introduced and intensively studied, inspiring novel applications in electronics including thin-film transistors and chemical-gas sensing [1–8]. For example, black phosphorus (BP) is one of the prominent 2D materials of recent interest for transistor applications, with its relatively high mobility, large in-plane anisotropy and tunable direct bandgap [9–13], finding applications in gas sensing [14] as well as infrared emission [15]. A second example, exfoliated Bi_2Se_3, is a topological insulator in bulk form, but becomes a narrow-gap semiconductor in its 2D form [16] and shows promise for gas sensing given its recently demonstrated air stability [6, 17, 18]. Due to the large surface-area-to-volume ratio, the physical properties of 2D materials are significantly affected by the disorder potential of the surrounding environment. And whereas disorder needs to be minimized in high-mobility transistors, disorder serves as an indicator of the type and amount of surface absorbates in sensors. In either case, disorder needs to be properly characterized, given the large number of possible scattering sources that includes substrate roughness, exposure to residual chemicals during cleaning [19–21], metal doping [22, 23], encapsulation [24, 25] and surface functionalization [26, 27].

Ionized impurities, in particular, present a two-fold effect on the mobility of 2D materials. On the one hand, the Coulomb scattering from the ions reduces the mobility, where the amount of the Coulomb

© 2022 IOP Publishing Ltd

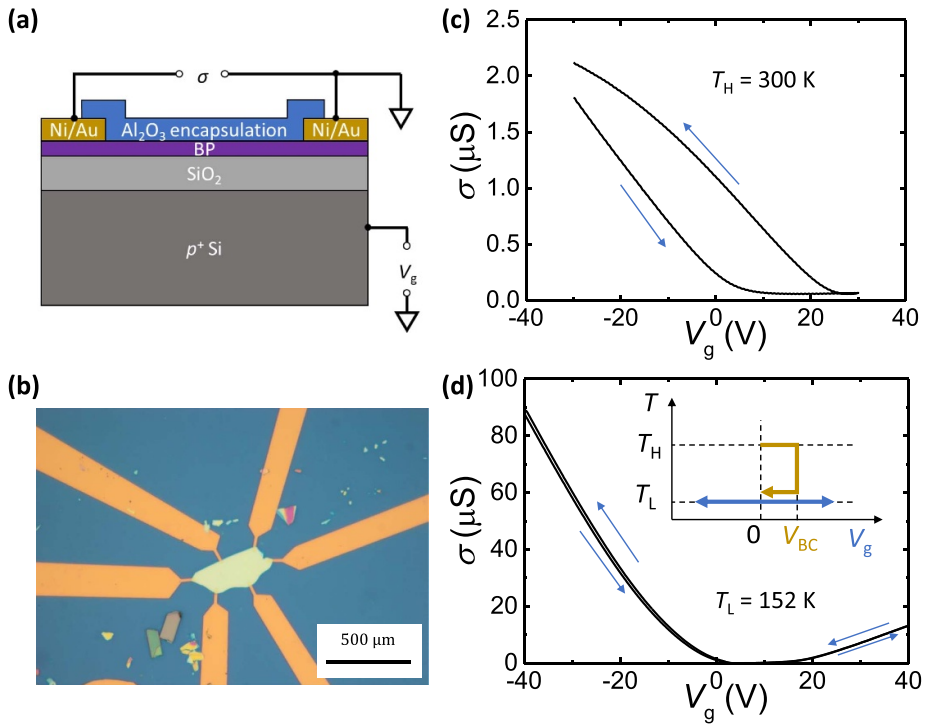

Figure 1. Device structure and hysteretic behavior of the gate voltage sweep. (a) Schematic illustration of the device structure. The BP flake is exfoliated onto a heavily p-doped Si/SiO_2 substrate. Ni/Au contacts are deposited on the BP flake. After intentional oxidization, Al_2O_3 is deposited to encapsulate the sample to prevent further oxidization. (b) Microscopic image of a typical sample. (c) Room temperature gate voltage sweep of a typical sample, showing clear hysteretic behavior. (d) After the sample is cooled down to $T_L = 152$ K, the gate voltage sweep is measured again, which shows the hysteresis being suppressed at low temperature. At $T_L = 100$ K, the hysteresis diminishes completely. Panel (d) inset show a diagram of the bias cooling process where the sample is first biased at room temperature to the bias cooling voltage V_{BC}, then the sample is cooled down to T_L under this V_{BC}, and finally, the voltage is withdrawn after T_L is reached (yellow). The gate voltage is subsequently swept at low temperature between circa $V_g = -25$ to 25 V (blue).

scattering is proportional to the density and charge of ionized traps. On the other hand, the constraint of charge neutrality correlates the density of ions with the density of free carriers, which, in turn, further increases or decreases the amount of disorder screening to either enhance or suppress mobility depending on the sign of the ionic charge relative to that of the free carriers.

In this Letter, a two-dimensional conductivity scaling (2DCS) analysis is proposed that can be generalized for any 2D material systems with tunable impurity density. The analysis is applied here in two case studies: a BP multilayer and a Bi_2Se_3 monolayer flake, whereby different concentrations of ionized impurity scatterers are configured in the same device, and the free charge carrier density further tuned via the field effect with a back-gate. The experimental gate-dependent conductivity curves for each sample are observed to collapse onto a single distinctive conductivity curve upon scaling the conductivity by a factor r and simultaneously shifting the gate bias by V_s for different impurity concentrations. This scaled conductivity versus gate bias characteristic extends over a far larger range of gate voltages than is normally accessible in a single sample, allowing one to access and distinguish a broader range of mobility-limiting regimes, such as ionized impurity scattering or interface scattering. The slope of the 2DCS scaling parameter plot, which we call the disorder charge specific scattering rate $\Gamma_q \equiv \mathrm{d}r/\mathrm{d}V_s$, gives a measure of the scattering strength per unit density of signed impurity charge, and identifies the ionized impurities as predominantly negatively charged (acceptor-like) $\Gamma_q < 0$ or positively charged (donor-like) $\Gamma_q > 0$.

We first consider the gated BP device with intentional surface oxidization, in which the ionized impurity concentration can be tunably controlled via bias cooling. The BP sample is fabricated by micromechanically exfoliating BP flakes onto a degenerately doped Si wafer with a 300 nm thermal SiO_2 film (figure 1(a)). The sample (BP thickness $d = 13$ nm) is intentionally exposed to the ambient air with 75% relative humidity for 12 h, then encapsulated with 10 nm Al_2O_3 deposited by atomic layer deposition to protect the top surface from further oxidization after the deposition of electrodes of Ni/Au 10/40 nm [24]. The surface oxidization intentionally introduces deep charge traps near the conducting channel of the sample. The microscopic image of a typical sample is shown in figure 1(b). Room temperature conductivity versus gate voltage sweep of typical device shows a large hysteresis loop in figure 1(c) which is known to arise in gated systems which possess deep charge traps, making the sample's room

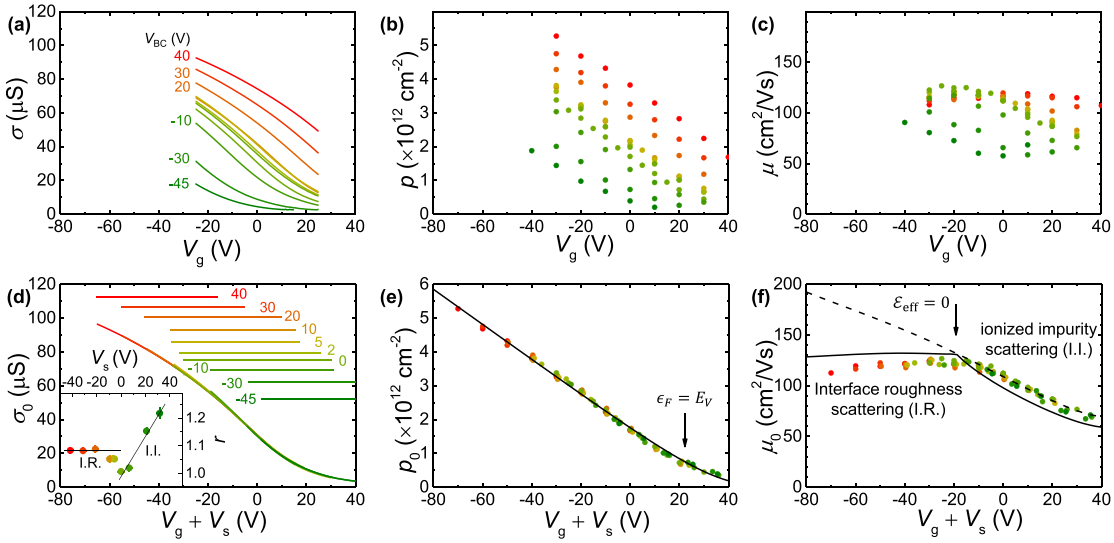

Figure 2. Raw transport data from the BP sample at $T_L = 100$ K (top row) and the corresponding scaled transport curves (bottom row). Dependence of (a) conductivity σ, (b) carrier concentration p, and (c) mobility μ vs. gate voltage V_g for different bias cooldown voltages V_{BC}. Dependence of (d) scaled conductivity σ_0, (e) unscaled carrier concentration p_0, and (f) scaled mobility μ_0 vs. shifted gate voltage $V_g + V_s$. The horizontal lines in panel (d) show the shifted ranges of the raw conductivity σ data indicating large overlaps between the shifted curves. In panel (e), the calculated hole density (black solid line) agrees with the data with degeneracy crossover indicated by the arrow at $\epsilon_F = E_V$. In panel (f), the calculated mobility (black solid line) explains the main features of the data, combining ionized impurity scattering (dashed line) with interface roughness scattering. The kink at $V_g + V_s = -20$ V is an artifact of the diverging power law interface roughness scattering, indicated by the arrow at $\mathcal{E}_{eff} = 0$. The 2DCS parameters r vs. V_s are summarized in panel (d) inset, where the sloped black lines indicate the disorder charge specific scattering rate $\Gamma_q \equiv dr/dV_s$. $\Gamma_q = 0$ indicates scattering that is insensitive to doping by remote ionized impurities, namely interface roughness scattering (I.R.). Positive $\Gamma_q > 0$ indicates donor-like positively ionized impurity scattering (I.I.). The confidence interval, when larger than the symbol size, is shown as horizontal and vertical error bars.

temperature performance difficult to characterize due to transient relaxation [13]. In bulk semiconductors, this hysteresis would be reminiscent of deep-level transient spectroscopy (DLTS) [28] where a temperature sweep under pulsed bias would reveal a distribution of activation energies. Here, we introduce an alternate method of deducing electrostatic information about the charge traps whereby the deep traps are charged at room temperature and then that trap charge is frozen in place at low temperature.

Gate-bias cooling allows the ionized impurity density to be controlled. Following standard protocol as defined in other systems [29–32], at room temperature the sample is held under a fixed gate bias V_{BC}, allowing the charge trap states near the BP layer to equilibrate with the local biased chemical potential of the conducting BP layer. Then the sample is cooled to low temperature $T_L = 100$ K with this fixed bias-cooling voltage V_{BC}, freezing the trapped charge into place. The low temperature also eliminates any hysteresis, so the bias cooling voltage V_{BC} can be withdrawn at low temperature and the gate bias swept in the presence of the trapped charge characteristic of that cool-down voltage, shown in figure 1(d) inset. Transport properties are then measured as a function of the gate bias V_g sweep at low temperature. The absence of hysteresis in figure 1(d) allows a thorough analysis of gated conductivity for different charge states of the traps, allowing the role of the traps themselves to be electrostatically distinguished in this Letter. This bias cooling experiment is repeated multiple times for the same device at different bias cooling voltages V_{BC}.

With a systematic series of bias-cooling voltages V_{BC}, the same device can be prepared with controllably different concentrations of ionized scatterers. The corresponding gate-dependent conductivity curves σ can be collected as shown in figure 2(a). The overall negative slope of conductivity versus gate bias suggests p-type conduction, as expected. Aside from that, these curves have quantitatively and qualitatively different lineshapes, especially comparing curves of extreme bias-cooling voltages V_{BC}, and at first glance appear to have little in common. High conductivities tend to show negative curvature, intermediate conductivities are approximately linear, and low conductivities have positive curvature versus gate bias V_g. Such a complex set of curves reflects that the underlying mobility is dominated by different effects under different cool-down conditions and different gate biases.

To further separate the carrier density and mobility from the conductivity, the Hall effect was measured at a sequence of gate voltages V_g for different bias cooling conditions V_{BC}. Low-temperature gate-dependent Hall effect measurements under different bias-cooling voltages V_{BC} determined the hole densities p shown in figure 2(b). The Hall mobility is then determined from figures 2(a) and (b) by dividing the

conductivity by the Hall density $\mu = \sigma/p$, plotted in figure 2(c). Other than the obvious reduction in hole density with increasing gate voltage confirming the p-type behavior in figure 2(b), it is difficult to see any systematic trend directly in the mobility data in figure 2(c) anymore than in the original conductivity plots of figure 2(a).

Careful inspection, however, reveals an interesting pattern that paves the way for further analysis. First, note that the $V_{BC} = 0$ curve of σ versus V_g in figure 2(a) has its inflection point near $V_g = 0$ V. But as V_{BC} increases, the gate voltage of the inflection point on the corresponding curve increases. If all curves with positive V_{BC} are shifted to the left and negative V_{BC} to the right, the inflection points can be aligned for all cooldowns. Moreover, if these horizontally aligned curves are subsequently scaled vertically, they collapse onto the original $V_{BC} = 0$ curve, as shown on figure 2(d). This scaled conductivity curve, $\sigma_0(V_g)$, can be expressed in terms of the i^{th} raw conductivity curve $\sigma_i(V_g)$, after a gate voltage shift $V_{s,i}$ and a mobility scaling by the factor r_i as follows,

$$\sigma_0(V_g) = r_i \sigma_i(V_g - V_{s,i}), \tag{1}$$

or equivalently, $\sigma_0(V_g + V_{s,i}) = r_i \sigma_i(V_g)$.

Furthermore, if the *same set of gate voltage shifts* $V_{s,i}$ are applied to the density data of figure 2(b), the resulting plot of figure 2(e) shows a similar collapse onto a single curve. Note that density is shifted, only, not scaled. It follows as a consequence that the Hall mobility will also scale to a single curve as in figure 2(f) by applying the same set of gate voltage shifts $V_{s,i}$ and scaling factors r_i. This empirical analysis reveals a distinctive behavior of the BP device that is common across different bias cooling voltages V_{BC}, with a compelling collapse of both conductivity and density for the same set of gate shifts $V_{s,i}$, begging a microscopic explanation.

The empirically observed bias cooling scaling law for the conductivity can be quantitatively explained with an ionized impurity scattering model, where charged ions act as both scatterers that decrease the mobility, and as ionized dopants that affect the free carrier density and therefore the screening of the impurity potential [13]. At gate voltages where charged impurity scattering is the principal mobility-limiting mechanism [33], the elastic momentum relaxation time τ can be written out explicitly using the Fermi's golden rule under the Thomas-Fermi screening approximation [34]. Assuming an isotropic system with remote ionized impurities separated by distance d from the conducting channel, the energy-dependent transition rate can be written following the standard angular integral [35],

$$\frac{1}{\tau(\epsilon)} = \frac{e^*_{imp} n_{imp} m^*}{\pi \hbar^3} \oint \left(\frac{2\pi e e^{-2k(\epsilon)\sin\frac{\theta}{2} d}}{k(\epsilon)\sin\frac{\theta}{2}\kappa + \pi e^2 g_{2D}} \right)^2 \times (1 - \cos\theta) d\theta = \frac{n_{imp}}{\tilde{\tau}(\epsilon)}, \tag{2}$$

where ε is the majority carrier's kinetic energy ($\epsilon = E - E_C$ for electrons, and $\epsilon = E_V - E$ for holes), θ is the scattering angle between initial and final states $|\vec{k}\rangle$ and $|\vec{k'}\rangle$, κ is the dielectric constant, n_{imp} is the sheet density of charged impurities, e^*_{imp} is the effective charge of each impurity, and $g_{2D} = m^*/(\pi\hbar^2)$ is the 2D density of states of the free carriers. In the rightmost equation, $1/\tilde{\tau}(\epsilon)$ represents the kinetic energy-dependent scattering rate induced by a unit density of ionized impurities.

For elastic scattering in 2D, the average mobility as a function of the Fermi energy $\mu(\epsilon_F)$ can then be determined as a weighted average of the energy-dependent scattering with the derivative of Fermi function [35]:

$$\mu(\epsilon_F) = \frac{1}{n_{imp}} \frac{e}{\pi p(\epsilon_F)\hbar\sqrt{2m^*}} \int_0^\infty \tilde{\tau}(\epsilon)\epsilon^{1/2} \times \left[-\frac{\partial f_{FD}(\epsilon - \epsilon_F)}{\partial \epsilon} \right] d\epsilon = \frac{\tilde{\mu}(\epsilon_F)}{n_{imp}}, \tag{3}$$

with the majority carrier Fermi–Dirac distribution function $f_{FD}(\epsilon) = (1 + e^{\epsilon/k_B T})^{-1}$. In the rightmost equation, $\tilde{\mu}(\epsilon_F)$ represents the average carrier mobility induced by a unit density of ionized impurities, which depends only on the Fermi energy ϵ_F for a given temperature. The hole density p for a single subband can be expressed solely as a function of ϵ_F with the density-of-states integral,

$$p(\epsilon_F) = g_{2D} \int_0^\infty f_{FD}(\epsilon - \epsilon_F) d\epsilon. \tag{4}$$

As a consequence, the total conductivity $\sigma(\epsilon_F, n_{imp})$ can be expressed as a function of only the Fermi energy and the impurity density,

$$\sigma(\epsilon_F, n_{imp}) = p(\epsilon_F) \frac{\tilde{\mu}(\epsilon_F)}{n_{imp}} = \frac{\tilde{\sigma}(\epsilon_F)}{n_{imp}}, \tag{5}$$

where $\tilde{\sigma}(\epsilon_F)$ is defined as the conductivity for a unit density of ionized impurities.

From these definitions, a set of concise equations can be used to describe the sample's behavior under different charged impurity states. Note that when the density n_{imp} of ionized impurities is reconfigured with different bias coolings, the electron's Fermi energy ϵ_F also changes due to the constraint of charge neutrality. If the ionized impurity-induced change in density for the i^{th} bias cooling results in a gate voltage shift $V_{s,i}$, the expression for the Fermi energy will depend only on the capacitive effect of the gate voltage V_g and this additional voltage shift $V_{s,i}$ in the following manner,

$$\epsilon_F[p_i(V_g - V_{s,i})] = \epsilon_F(V_g - V_{s,i}). \quad (6)$$

Inserting equation (6) into equation (5), one recovers the empirical scaling law in equation (1), exemplified in the 2DCS conductivity plot of figure 2(d). A positive $V_{s,i}$ therefore corresponds to a positive net change in ionized impurity concentration. Thus $V_{s,i} > 0$ signifies either an increase in donor-like or decrease in acceptor-like ionized impurity concentrations, or both. Analogous to equation (1), where the subscript '0' represents the universal curve as extended from the zero-bias cooldown, the scaling laws for the hole density and mobility of figures 2(e) and (f), respectively, map on top of the zero-bias cooling data as,

$$p_0(V_g) = p_i(V_g - V_{s,i}), \quad (7)$$

$$\mu_0(V_g) = r_i\mu_i(V_g - V_{s,i}), \quad (8)$$

where $r_i = n_{imp,i}/n_{imp,0}$ can now be understood as the charged impurity density ratio of the i^{th} cooldown relative to that at zero-bias cooldown. Note that the scaling factor r is inversely proportional to the ionized impurity density, which is in turn determined by the bias cooling voltage V_{BC}. We refer to this method as the two-dimensional conductivity scaling (2DCS) analysis.

With the 2DCS analysis justified above, the plots of figures 2(d)–(f) can reveal more information about the sample at hand. The easiest way to read these normalized plots is to assume a zero-bias cooldown whereby $V_s = 0$, allowing the horizontal axis to simply represent the gate voltage V_g, but with an expanded range. First, the hole density will be considered in the plot of figure 2(e) where a transition is evident between degenerate and non-degenerate doping. As the normalized gate voltage $V_g + V_s$ increases from −40 to 40 V, the hole density decreases linearly at first, then shows upwards curvature in the rightmost tail. The linear behavior is expected for a simple capacitive model with degenerate hole density, and the transition to an exponential tail is expected when the hole density becomes non-degenerate. Applying the analysis of Zhu *et al* [36] (see supplementary note 1 (available online at stacks.iop.org/TDM/9/031002/mmedia)), the predicted density with gate voltage is plotted with black solid line in figure 2(e), assuming a constant energy density of states for the ionized impurity scatterers of 5.2×10^{10} cm^{-2} meV^{-1} and a geometric capacitance due to the 300 nm SiO_2. The crossover point $\epsilon_F = E_V$ is indicated with an arrow, and the overall curve shows excellent agreement with the data revealing useful information about the doping degeneracy that cannot be gleaned without the 2DCS analysis.

The mobility limiting mechanisms can also be determined from the 2DCS analysis via the scaled mobility μ_0 plot of figure 2(f). There is a clear cross-over from $V_g + V_s < 0$ where mobility is largely independent of gate voltage to $V_g + V_s > 0$ where mobility decreases with increasing normalized gate voltage.The dashed line in figure 2(f) represents ionized impurity scattering according to equation (3) assuming uniformly distributed scatterers of charge $e^* = e$ within $d = 1$ nm of the conducting channel with a density of $n_{imp,0} = 6.2 \times 10^{12}$ cm^{-2}. The free carrier density $p(\epsilon_F)$ in the Thomas-Fermi screening in equation (3) assumes the same gate-dependent carrier density as the solid fit curve $p_0[\epsilon_F(V_g + V_s)] = p_0(V_g + V_s)$ in figure 2(e). Under positive gate bias, the scaled mobility of figure 2(f) follows the dashed line suggesting that ionized impurity scattering dominates here. But for $V_g + V_s < -20$ V, the mobility deviates further from the ionized impurity curve, likely due to the interface roughness scattering [33] with the holes being attracted to the BP/SiO_2 interface under negative substrate gate bias. Interface roughness would contribute a mobility term with power-law dependence on the absolute value of the average electric field in the BP layer, $\mu_{SR} \propto |\mathcal{E}_{eff}|^{-\alpha}$. Following Matthiessen's rule, the total mobility $\mu_{tot} = (\mu_{imp}^{-1} + \mu_{SR}^{-1})^{-1}$ is plotted with a solid black line in figure 2(f), fitting the measured data reasonably well with $\alpha = 0.8$. Note that the the kink indicated by an arrow at the crossover $V_g + V_s = -20$ V in figure 2(f) is consequence of the power-law divergence of the interface roughness scattering when the average electric field in the BP layer vanishes, $\mathcal{E}_{eff} = 0$.

This mobility crossover is doubly confirmed in the 2DCS parametric plot of r vs. V_s in the inset of figure 2(d). Towards the right of the inset, a positive voltage shift $V_s > 0$ is accompanied by an increase in the scattering strength r. This implies that the scattering potential increases as the ionized impurity charge becomes more positive, thus ionized impurities are predominantly donor-like positive charges. This behavior can be quantified by defining the slope $\Gamma_q \equiv dr/dV_s$ as a disorder-charge specific scattering rate which carries the same sign as the dominant impurity ions. The predominance of ionized impurity scattering is consistent with the previously identified mobility regime to the right of figure 2(f) for $V_g + V_s > 0$ ($V_{BC} < 0$). On the other hand, in the figure 2(d) inset for $V_s < 0$, the scattering strength identified by r appears to be fixed independent of any change in ionized impurity charge. This zero slope $\Gamma_q = 0$ suggests mobility dominated by a charge-neutral scattering mechanism. This is again consistent with the left side of figure 2(f) where the interface roughness scattering has a significant contribution. And whereas the standard mobility analysis of figure 2(f) requires an external magnetic field to collect Hall effect data, the parametric plot of r vs. V_s can be generated simply by device operation at different impurity doses, thereby greatly simplifying mobility analysis via examination of the slope of this parametric plot Γ_q. The error analysis in figure 2(d) inset show

that all but one of the 2DCS parameters have negligible error. As per supplementary note 2, as long as the gate voltage sweeps clearly deviate from an exponential curve, the 2DCS analysis will be valid.

Another important application of 2D materials where the 2DCS analysis shows its relevance is in gas sensing devices. To study ionized impurity potentials induced by adsorbed gases, gate-dependent conductivity curves of a monolayer Bi_2Se_3 sample were investigated. In this case, the disorder potential is tuned by desorbing or adsorbing different amounts of ambient gas. Here no Hall effect studies are conducted, but as described above, the 2DCS analysis can still be applied to yield insightful results about the nature of the scattering. The monolayer Bi_2Se_3 on a 300 nm SiO_2 substrate was prepared by the evaporative thinning method [21]. Four parallel Cr/Au 5 nm/50 nm contacts were defined by e-beam lithography and deposited by thermal evaporation. The sample was then put into a home-built reducing chamber for *in-situ* electrical measurements. After being annealed in forming gas (H_2:N_2 = 5:95) at $T = 400$ K, it was then cooled down to $T = 300$ K and the gate-dependent conductivity was measured at quasi-equilibrium intervals during a gas adsorption sequence, first under vacuum, and then with forming gas, and finally ambient air with relative humidity around 25%. The measurement time scale is much faster than the gas adsorption process, allowing these quasi-equilibrium gate sweep to characterize the instantaneous state of the sample.

The conductivity curves under gate voltage sweep are shown in figure 3(a). In the initialized state after high temperature desorption, the intrinsic *n*-type conduction was observed as evidenced by a positive slope in the gate-dependent conductivity. The *n*-type conductivity was seen to slowly increase on hour-long time scales as measured from subsequent gate sweeps taken at later intervals as the sample stayed at $T = 300$ K in a nominal vacuum. One would expect that under vacuum any gas adsorbates would slowly desorb, consistent with this increase in conductance. After being exposed to the forming gas and then to air, the conduction showed the opposite effect, changing from *n*-type to *p*-type while the conductivity kept decreasing significantly with longer exposure time within the entire exposure process. As with the case of BP, from the raw data of figure 3(a) alone, it is difficult to make any definitive conclusions about the system, since the reduced conduction caused by the forming gas and air could, in principle, be reducing the mobility, the carrier density, or both.

Following the 2DCS analysis protocol, the resulting scaled gate-dependent conductivity curve is shown in figure 3(b). As shown in figure 3(b) inset, the mobility scaling factor r increases by an order of magnitude as V_s decreases over the entire range. From the slope of the conductivity curves with gate bias in figure 3(a), we can tell that the carrier transitions all

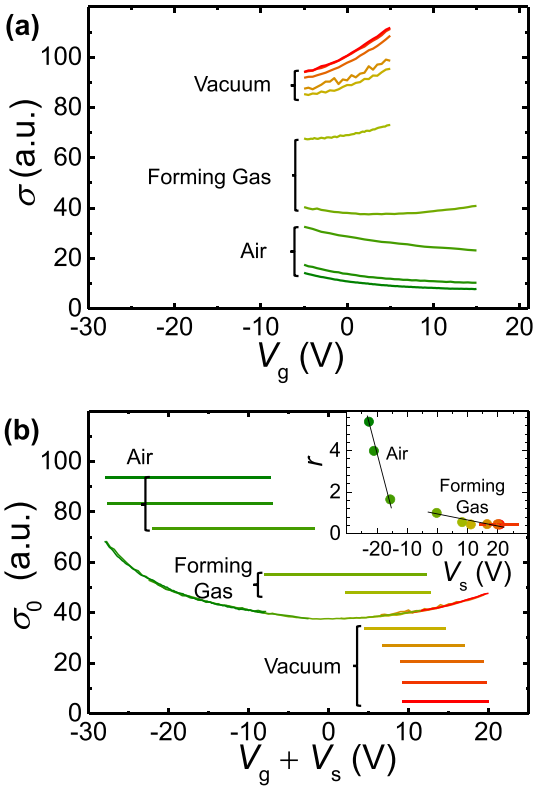

Figure 3. 2DCS analysis for the Bi_2Se_3 sample. (a) Gate-dependent conductivity curves at room temperature with different adsorbate conditions. (b) The scaled conductivity data on a single curve. The 2DCS parameters r versus V_s are shown in panel (b) inset. The confidence interval, when larger than the symbol size, is shown as horizontal and vertical error bars. The negative slope is indicative of acceptor-like adsorbates predominantly ionized with negative charge. The steep slope for the specific scattering $\Gamma_q \equiv dr/dV_s$ under air versus the shallow slope under forming gas and vacuum indicate different scattering strengths per net charge for different gas adsorption conditions.

the way from *n*-type with positive slope $d\sigma/dV_g > 0$ to *p*-type with negative slope $d\sigma/dV_g < 0$. Meanwhile, the increase in mobility scaling factor r in the figure 3(b) inset as the sample goes from vacuum to ambient gas indicates that the disorder strength increases under continued exposure to adsorbates, even after the conduction channel changed to *p*-type.

As per our general 2DCS arguments, this disorder-charge specific scattering rate Γ_q shown with negatively sloped black lines in the r vs. V_s parameter plot (figure 3(b) inset) corresponds to acceptor-like disorder: an increased number of impurities corresponds to an increasing hole (decreasing electron) concentration. While the sign of the specific scattering Γ_q shows the charge type of the dominant impurities, the magnitude of the slope Γ_q is indicative of the ionized impurity species. For cases where the sample is under vacuum or forming gas where $V_s > -10$ V, the specific scattering Γ_q has a small negative value, indicating that large changes in the impurity-induced doping result in small changes in the mobility. Conversely, when the sample is exposed

to air, $V_s < -10$ V, the specific scattering Γ_q takes a large negative value.

The scenario for gas sensing is different from that of bias cooling, because multiple gas species may or may not all have the same sign and magnitude of effective charge e^*. Density functional theory predicts typical charge transfer values for common gas molecules to span both positive and negative values around $-0.6e \lesssim e^* \lesssim -0.6e$, and the sign and amplitude of the charge transfer is very much dependent on the exact chemistry of the interface material [37–40]. Equation (3) then is modified according to Mathiessen's rule with an impurity contribution for each gas species:

$$\frac{1}{\mu(\epsilon_F)} = \frac{n_{imp,1}}{\tilde{\mu}_1(\epsilon_F)} + \frac{n_{imp,2}}{\tilde{\mu}_2(\epsilon_F)} + \ldots, \tag{9}$$

so that the mobility decreases as each new species of ionized impurity is added. However, note that the voltage shift V_s in equation (6) will also be modified once multiple species of impurities are involved:

$$\epsilon_F[p_i(V_g - V_{s,i}^{(1)} - V_{s,i}^{(2)} \ldots)] = \epsilon_F(V_g - V_{s,i}^{(1)} - V_{s,i}^{(2)} \ldots), \tag{10}$$

and positively charged impurities $e^* > 0$ will contribute a positive V_s and negatively charged $e^* < 0$ a negative V_s. For example, in a simplified scenario with two species of adsorbed gases with opposite charge N_D^+ and N_A^-, then the conductivity magnitude varies as the sum of the impurity densities $r \sim N_D^+ + N_A^-$, whereas the voltage shift will have competing positive and negative contributions $V_s \sim N_D^+ - N_A^-$. A large amplitude of the specific scattering $|\Gamma_q| = |dr/dV_s|$ can therefore result from dopant compensation since the total number of impurities may be large leading to a large scattering parameter r in the numerator, whereas the net impurity charge may be small leading to small V_s shifts in the denominator. Note that a large Γ_q is observed in figure 3(b) inset at large negative V_s in the presence of air, where the gases O_2 and water vapor are present. Such observations highlight the utility of the 2DCS method to identify traits of the adsorbed scatterers, helping to address the long-standing cross-sensitivity issue of distinguishing different gases in gas sensing 2D devices [7].

In conclusion, the proposed 2DCS method can characterize scattering in 2D materials when the scattering potential consists of a tunable concentration of ionized impurity scatterers, such as charge traps or gas adsorbates. From the analysis presented here, one can extract a 2DCS scaled conductivity curve and deduce a 2DCS parameter plot of the scaling parameter r versus the shift V_s. Examination of trends in these two parameters allows one to separate relative contributions to the mobility through the slope of this plot, defined as the disorder charge specific scattering rate $\Gamma_q \equiv dr/dV_s$. This parameter reveals whether the dominant impurities are acceptor-like ($\Gamma_q < 0$) or donor-like ($\Gamma_q > 0$), and even quantify relative levels of scattering strength per unit impurity charge and/or compensation. The characteristic conductivity curve $\sigma_0(V_g + V_s)$ allows one to determine the conductivity for a broad range of impurity doping and gate voltage biases. The proposed 2DCS analysis will be useful for analyzing gate-tunable 2D materials which undergo oxidation, annealing, and surface doping such as for gas sensors and will provide a diagnostic test for comparing differently prepared samples to aid in device optimization. Following the analysis outlined in this Letter, one would also be able to expand the same principle demonstrated here on a single device and consider an impurity dosage study for 2D materials, or calibrate 2D gas sensors to differentiate multiple gas species from their 2DCS fingerprint, for example.

Data availability statement

The data that support the findings of this study are available upon reasonable request from the authors.

Acknowledgements

The authors thank Alek Jansen for helping setup the reducing chamber. This research was supported by the Air Force Office of Scientific Research (FA95501510247 and FA05501510377) and the National Science Foundation Materials Research Science and Engineering Center (MRSEC) of Northwestern University (DMR-1121262 and DMR-1720139). This work made use of the EPIC facility of Northwestern University's NUANCE Center, which has received support from the Soft and Hybrid Nanotechnology Experimental (SHyNE) Resource (NSF ECCS-1542205); the MRSEC program (DMR-1720139) at the Materials Research Center; the International Institute for Nanotechnology (IIN); the Keck Foundation; and the State of Illinois, through the IIN.

ORCID iDs

Chulin Wang https://orcid.org/0000-0002-1877-3445
Lawrence A Rhoads https://orcid.org/0000-0002-7391-7333
Mark C Hersam https://orcid.org/0000-0003-4120-1426
Matthew A Grayson https://orcid.org/0000-0003-4914-5043

References

[1] Novoselov K S, Geim A K, Morozov S V, Jiang D, Zhang Y, Dubonos S V, Grigorieva I V and Firsov A A 2004 Electric field effect in atomically thin carbon films *Science* **306** 666–9
[2] Geim A K and Novoselov K S 2007 The rise of graphene *Nat. Mater.* **6** 183–91

[3] Bhimanapati G R *et al* 2015 Recent advances in two-dimensional materials beyond graphene *ACS Nano* **9** 11509–39

[4] Chhowalla M, Jena D and Zhang H 2016 Two-dimensional semiconductors for transistors *Nat. Rev. Mater.* **1** 16052

[5] Chiang C-C, Ostwal V, Wu P, Pang C-S, Zhang F, Chen Z and Appenzeller J 2021 Memory applications from 2D materials *Appl. Phys. Rev.* **8** 021306

[6] Yang S, Jiang C and Wei S-H 2017 Gas sensing in 2D materials *Appl. Phys. Rev.* **4** 021304

[7] Buckley D J, Black N C, Castanon E G, Melios C, Hardman M and Kazakova O 2020 Frontiers of graphene and 2D material-based gas sensors for environmental monitoring *2D Mater.* **7** 032002

[8] Carvalho A, Wang M, Zhu X, Rodin A S, Su H and Neto A H C 2016 Phosphorene: from theory to applications *Nat. Rev. Mater.* **1** 16061

[9] Liu H, Neal A, Zhu Z, Luo Z, Xu X, Tománek D and Ye P 2014 Phosphorene: an unexplored 2D semiconductor with a high hole mobility *ACS Nano* **8** 4033

[10] Xia F, Wang H and Jia Y 2014 Rediscovering black phosphorus as an anisotropic layered material for optoelectronics and electronics *Nat. Nanotechnol.* **5** 4458

[11] Li L *et al* 2017 Direct observation of the layer-dependent electronic structure in phosphorene *Nat. Nanotechnol.* **12** 21–25

[12] Peng L, Wells S A, Ryder C R, Hersam M C and Grayson M 2018 All-electrical determination of crystal orientation in anisotropic two-dimensional materials *Phys. Rev. Lett.* **120** 086801

[13] Aygen C C, Peng L, Luo J, Wells S A, Hersam M C and Grayson M Characterization of gate induced heavy-tail hysteresis transients in 2D materials (in preparation)

[14] Cui S, Pu H, Wells S A, Wen Z, Mao S, Chang J, Hersam M C and Chen J 2015 Ultrahigh sensitivity and layer-dependent sensing performance of phosphorene-based gas sensors *Nat. Commun.* **6** 8632

[15] Husko C *et al* 2018 Silicon-phosphorene nanocavity-enhanced optical emission at telecommunications wavelengths *Nano Lett.* **18** 6515–20

[16] Zhang Y *et al* 2010 Crossover of the three-dimensional topological insulator Bi_2Se_3 to the two-dimensional limit *Nat. Phys.* **6** 584

[17] Late D J *et al* 2013 Sensing behavior of atomically thin-layered MoS_2 transistors *ACS Nano* **7** 4879–91

[18] Perkins F K, Friedman A L, Cobas E, Campbell P, Jernigan G and Jonker B T 2013 Chemical vapor sensing with monolayer MoS_2 *Nano Lett.* **13** 668–73

[19] Morozov S, Novoselov K, Katsnelson M, Schedin F, Elias D, Jaszczak J A and Geim A 2008 Giant intrinsic carrier mobilities in graphene and its bilayer *Phys. Rev. Lett.* **100** 016602

[20] Cheng Z, Zhou Q, Wang C, Li Q, Wang C and Fang Y 2011 Toward intrinsic graphene surfaces: a systematic study on thermal annealing and wet-chemical treatment of SiO2-supported graphene devices *Nano Lett.* **11** 767–71

[21] Huang Y-K, Cain J D, Peng L, Hao S, Chasapis T, Kanatzidis M G, Wolverton C, Grayson M and Dravid V P 2014 Evaporative thinning: a facile synthesis method for high quality ultrathin layers of 2D crystals *ACS Nano* **8** 10851–7

[22] McChesney J L, Bostwick A, Ohta T, Seyller T, Horn K, González J and Rotenberg E 2010 Extended van Hove singularity and superconducting instability in doped graphene *Phys. Rev. Lett.* **104** 136803

[23] Han C *et al* 2017 Surface functionalization of black phosphorus via potassium toward high-performance complementary devices *Nano Lett.* **17** 4122–9

[24] Wood J D, Wells S A, Jariwala D, Chen K-S, Cho E, Sangwan V K, Liu X, Lauhon L J, Marks T J and Hersam M C 2014 Effective passivation of exfoliated black phosphorus transistors against ambient degradation *Nano Lett.* **14** 6964–70

[25] Zomer P, Guimarães M, Brant J, Tombros N and Van Wees B 2014 Fast pick up technique for high quality heterostructures of bilayer graphene and hexagonal boron nitride *Appl. Phys. Lett.* **105** 013101

[26] Wang X, Xu J-B, Xie W and Du J 2011 Quantitative analysis of graphene doping by organic molecular charge transfer *J. Phys. Chem.* C **115** 7596–602

[27] Ryder C R, Wood J D, Wells S A, Yang Y, Jariwala D, Marks T J, Schatz G C and Hersam M C 2016 Covalent functionalization and passivation of exfoliated black phosphorus via aryl diazonium chemistry *Nat. Chem.* **8** 597–602

[28] Lang D 1974 Deep-level transient spectroscopy: a new method to characterize traps in semiconductors *J. Appl. Phys.* **45** 3023–32

[29] Singh A K and Gupta A K 2017 Reversible control of doping in graphene-on-SiO2 by cooling under gate-voltage *J. Appl. Phys.* **122** 195305

[30] Liang Y, Dong Q, Cheng M, Gennser U, Cavanna A and Jin Y 2011 Insight into low frequency noise induced by gate leakage current in AlGaAs/GaAs high electron mobility transistors at 4.2 K *Appl. Phys. Lett.* **99** 113505

[31] Long A, Pioro-Ladrière M, Davies J, Sachrajda A, Gaudreau L, Zawadzki P, Lapointe J, Gupta J, Wasilewski Z and Studenikin S 2006 The origin of switching noise in GaAs/AlGaAs lateral gated devices *Physica* E **34** 553–6

[32] Mooney P 1990 Deep donor levels (DX centers) in III-V semiconductors *J. Appl. Phys.* **67** R1–R26

[33] Takagi S-i, Toriumi A, Iwase M and Tango H 1994 On the universality of inversion layer mobility in Si MOSFET's: part I-effects of substrate impurity concentration *IEEE Trans. Electron Devices* **41** 2357–62

[34] Liu Y, Low T and Ruden P P 2016 Mobility anisotropy in monolayer black phosphorus due to scattering by charged impurities *Phys. Rev.* B **93** 165402

[35] Jacoboni C 2010 *Theory of Electron Transport in Semiconductors: A Pathway From Elementary Physics to Nonequilibrium Green Functions* vol 165 (Berlin: Springer)

[36] Zhu W, Low T, Lee Y-H, Wang H, Farmer D B, Kong J, Xia F and Avouris P 2014 Electronic transport and device prospects of monolayer molybdenum disulphide grown by chemical vapour deposition *Nat. Commun.* **5** 3087

[37] Cai Y, Zhang G and Zhang Y-W 2017 Charge transfer and functionalization of monolayer InSe by physisorption of small molecules for gas sensing *J. Phys. Chem.* C **121** 10182–93

[38] Cai Y, Ke Q, Zhang G and Zhang Y-W 2015 Energetics, charge transfer and magnetism of small molecules physisorbed on phosphorene *J. Phys. Chem.* C **119** 3102–10

[39] Yue Q, Shao Z, Chang S and Li J 2013 Adsorption of gas molecules on monolayer MoS_2 and effect of applied electric field *Nanoscale Res. Lett.* **8** 1–7

[40] Tang X, Du A and Kou L 2018 Gas sensing and capturing based on two-dimensional layered materials: overview from theoretical perspective *Wiley Interdiscip. Rev.-Comput. Mol. Sci.* **8** e1361